Lawrence Berkeley National Laboratory

Title
Automated local bright feature image analysis of nuclear protein distribution identifies changes in tissue phenotype

Permalink
https://escholarship.org/uc/item/6cb4s27g

Authors
Knowles, David
Sudar, Damir
Bator, Carol
et al.

Publication Date
2006-02-01

Peer reviewed

Classification: Biological Sciences/Biophysics

Automated local bright feature image analysis of nuclear protein distribution identifies changes in tissue phenotype

David W. Knowles*‡, Damir Sudar*, Carol Bator-Kelly[†], Mina J. Bissell*, Sophie A. Lelièvre[†‡].

Biophysics and Cancer Biology Departments, Life Sciences Division, Lawrence Berkeley National Laboratory, 1 Cyclotron Road, Berkeley, California, 94720, USA; † *Department of Basic Medical Sciences and Cancer Center, Purdue University, 625 Harrison Street, West Lafayette, Indiana 47907-2026, USA.*

‡**Corresponding authors:** David W Knowles and Sophie A Lelièvre.

David W. Knowles
Biophysics Department
Life Sciences Division
Lawrence Berkeley National Laboratory
MS: 84R0171, 1 Cyclotron Road
Phone: 510 486 6082
E-mail: dwknowles@lbl.gov

Sophie A. Lelièvre
Purdue University
Basic Medical Sciences, LYNN
625 Harrison street
West Lafayette, IN 47907-2026
Phone: 765 496 7793; fax: 765 494 0781
E-mail: lelievre@purdue.edu

Manuscript information: 26 pages; 4 figures; 250 words; 41757 character counts (for the text)

Abbreviations[1]

---

[1] HMECs, human mammary epithelial cells; LBF, local bright feature; NuMA, nuclear mitotic apparatus protein; 3D, three-dimensional;

Abstract

The organization of nuclear proteins is linked to cell and tissue phenotypes. When cells arrest proliferation, undergo apoptosis, or differentiate, the distribution of nuclear proteins changes. Conversely, forced alteration of the distribution of nuclear proteins modifies cell phenotype. Immunostaining and fluorescence microscopy have been critical for such findings. However, there is an increasing need for quantitative analysis of nuclear protein distribution to decipher epigenetic relationships between nuclear structure and cell phenotype, and to unravel the mechanisms linking nuclear structure and function. We have developed imaging methods to quantify the distribution of fluorescently-stained nuclear protein NuMA in different mammary phenotypes obtained using three-dimensional cell culture. Automated image segmentation of DAPI-stained nuclei was generated to isolate thousands of nuclei from three-dimensional confocal images. Prominent features of fluorescently-stained NuMA were detected using a novel local bright feature analysis technique, and their normalized spatial density calculated as a function of the distance from the nuclear perimeter to its center. The results revealed marked changes in the distribution of the density of NuMA bright features as non-neoplastic cells underwent phenotypically normal acinar morphogenesis. In contrast, we did not detect any reorganization of NuMA during the formation of tumor nodules by malignant cells. Importantly, the analysis also discriminated proliferating non-neoplastic cells from proliferating malignant cells, suggesting that these imaging methods are capable of identifying alterations linked not only to the proliferation status but also to the malignant character of cells. We believe that this quantitative analysis will have additional applications for classifying normal and pathological tissues.

Introduction

The organization of proteins within the cell nucleus appears to play a central role in directing nuclear functions necessary for cell proliferation and differentiation (1,2). Several nuclear proteins have been reported to display a specific compartmentalization (e.g. within the nucleolus, nuclear domains, or chromatin), and distribution (e.g., diffuse or aggregated), which change during the cell cycle (3,4), upon a switch between proliferation and growth arrest (5), or following cell differentiation (6-9). Studies using three-dimensional (3D) culture of breast epithelial cells in the presence of laminin-rich extracellular matrix have revealed that the distribution of certain nuclear proteins is dependent also on tissue morphogenesis (5,10). These culture models mimic the formation of specific tissue structures, where cells display both the function and the spatial arrangement typically found in a given organ (11,12). As a consequence, 3D cell culture models are being recognized as the systems of choice for unraveling critical cellular events involved in the development of pathologies such as cancer (13).

The HMT-3522 cancer progression series of human mammary epithelial cells (HMECs), cultured in 3D, constitutes a physiologically relevant model for studying the relationship between cellular organization and gene expression in normal and malignant cells (5,14-17). In such cultures, non-neoplastic HMT-3522 S1 HMECs (18) reproduce the formation of phenotypically normal, tissue-like glandular structures referred to as acini (17). Acinar morphogenesis proceeds by stepwise events including a proliferation stage from days 1 to 6 of culture, followed by growth arrest and the formation of the baso-apical polarity axis. Upon completion of acinar morphogenesis at day 10, S1 cells are organized into spherical and hollow structures delineated by a basement membrane at their basal pole, and a lumen at their apical pole. On the other hand, malignant T4-2 cells, which were derived from S1 cells (19), continue

to proliferate, and form disorganized and invasive tumor-like nodules under the same culture conditions (17,20). The distribution of nuclear proteins including retinoblastoma protein Rb, splicing factor SRm160, and nuclear mitotic apparatus (NuMA) protein is remarkably different between S1 cells in the early stage of acinar morphogenesis and S1 cells in fully formed acini (5). NuMA is diffusely distributed within the nuclei of proliferating cells, but aggregates into foci of increasing size as cells arrest proliferation and complete acinar morphogenesis. Importantly, the distribution of NuMA in acinar S1 cells is similar to that observed in biopsies of normal breast tissue, indicating that the 3D model of acini formation reproduces physiologically relevant features of NuMA organization.

Earlier reports described the distribution of NuMA as a single aggregate in the center of the cell nucleus in different cell types undergoing apoptosis (21,22) and as diffuse in cells cultured under non-differentiating condition (i.e., on plastic surfaces producing a flat monolayer of cells) (5,23). NuMA has since been reported to be organized in distinct foci in differentiated muscle (24) and differentiated lens cells (8). Another report has shown an association between a more punctate distribution of NuMA and a higher susceptibility to apoptosis induction in lymphocytes (25). Thus, NuMA distribution appears highly dependent on cell and tissue phenotypes and, as such, it has been proposed to constitute a reliable indicator of cell behavior (5,21,25).

For decades, it has been known that cancer cells display alterations in nuclear size and chromatin organization (26,27). Yet despite extensive use of the cell nucleus as a central diagnostic tool in cancer, there is little information available regarding specific alterations in nuclear organization in neoplasia. Understanding the relationship between nuclear organization and cell behavior has gained recent attention because it may help decipher signaling and

structural events involved in differentiation and cancer (28). With the recent refinements in confocal imaging technology, three-dimensional high-resolution imaging has become a powerful method for recording subtle organizational features in the cell nucleus. However, although a number of recent techniques for the quantitative analysis of three-dimensional images have been reported (29-35), the availability and application of robust image analysis tools in biology remain in their infancy (26,36,37).

Here, we report the use of confocal imaging to record the changes in the pattern of NuMA staining in HMECs expressing different phenotypes, and the development of an image analysis technique to translate the visual observations of the complexity of NuMA staining into quantitative results. In the original report (5), NuMA organization was determined by manually measuring foci sizes. However, such measurements are not possible when NuMA is diffusely organized and do not take into account the spatial reorganization of NuMA that is apparent in the differentiated cells. To circumvent this we have developed the radial local bright feature (radial-LBF) analysis. In this method, regions of local brightness in images of fluorescently-immunolabeled NuMA are isolated by an adaptive LBF analysis technique. The density of local bright features is then calculated within a set of concentric, volumetric terraces that subdivide the nucleus radially from its periphery to its center. The distribution of the bright features of NuMA can be represented by a simple graph, which permits an easy quantification of the changes in the spatial organization of this protein associated with different mammary phenotypes. The method relies on the delineation of individual nuclei, and in order to analyze thousands of nuclei in a short period of time, we have also developed a novel automated, three-dimensional segmentation technique. Using the radial-LBF analysis, we measured a striking reorganization of NuMA during acinar morphogenesis; no such reorganization occurred during the formation of tumor-

like nodules. Importantly, the radial-LBF analysis of NuMA distribution permitted a clear discrimination also between proliferating non-neoplastic cells and proliferating malignant cells, which to our knowledge has not been achieved so far using other evaluation methods.

Results

Radial-LBF distribution analysis in phenotypically normal breast acinar cells reveals a peak of density of NuMA bright features centered on a shell located midway between the periphery and the center of the nucleus.

The organization of NuMA in the nucleus displays intricate spatial distributions that vary with cell and tissue phenotypes (5,8,25). Visual analysis of NuMA immunostaining showed the formation of bright NuMA foci in a sea of diffuse NuMA staining during acinar morphogenesis (5). To quantify the distribution of bright NuMA foci, we calculated the radial distribution of the density of NuMA bright features isolated with the LBF analysis (described in the Materials and Methods section) within the three-dimensional volume of each nucleus (Fig. 1a). S1-HMECs were cultured in 3D to induce phenotypically normal acinar morphogenesis where NuMA domains are most abundant. Acini were immunostained for NuMA and counterstained with DAPI (Fig. 1b and c). A segmentation mask, which describes the position and extent of individual nuclei in 3D, was created from the DAPI image (Fig. 1d). Bright NuMA features were isolated from diffuse staining in the NuMA image using the LBF analysis. To visualize the localized accumulation of NuMA foci in the nucleus, the resulting bright features were overlaid on the segmentation mask (Fig. 1e). This visualization indicated that the density of NuMA bright features was low at the periphery of the nucleus and varied with the depth, radially, into the nucleus. To quantify NuMA bright features, a distance transform was applied to the segmentation mask to subdivide each nuclear volume into a set of concentric terraces of equal thickness, starting at the nuclear perimeter (Fig. 1f). The distance transformed-segmentation mask was combined with the LBF image to calculate the variation of the relative density of NuMA bright features as a function of the relative radial distance measured from the perimeter

7

of the nucleus to its center. To demonstrate the consistency of this radial-LBF analysis, the radial

distribution was plotted for 77 nuclei analyzed within a single image (Fig. 1a, graph). As the

visual representation indicated (Fig. 1e), the density of NuMA bright features was below average

at the perimeter of the nuclei. And as the radial depth into the nucleus increased, the density of

bright features increased and reached a peak, above the average density, at radial distance

0.55±0.05. Then the density decreased to a value close to the average density as the center of the

nucleus was reached.

The distribution of NuMA bright features changes as a function of acinar morphogenesis.

Previous analysis of the distribution of NuMA in S1 HMECs during the cell proliferation

stage (day 3 of 3D culture) and upon acinar differentiation (day 10 of 3D culture), suggested that

there was an increase in the foci-like aggregation of NuMA upon completion of acinar

morphogenesis (5). This analysis was based on visual estimation and the manual measurement of

the size of NuMA foci on images of NuMA staining. To assess the efficiency of the radial-LBF

analysis in measuring the changes in NuMA distribution reproducibly along the morphogenesis

process, we analyzed images of S1 HMECs cultured in 3D as a function of time, over a period of

12 days. At day 3, the density of NuMA bright features was the highest in a region towards the

perimeter of the nucleus (Fig. 2). After 10 days of culture, there was a clear reorganization of

NuMA away from the perimeter and towards the center of the nucleus (Fig. 2). This

reorganization was accompanied by a significant decrease of the density of NuMA bright

features at the perimeter of the nucleus. Visual inspection of images of NuMA distribution in

acinar cells showed that this protein was usually absent from regions located at the periphery of

the nucleus (Fig. 3). Similar density distributions were obtained with two different antibodies

directed against NuMA (not shown). To establish the statistical significance of the differences measured for NuMA distribution between proliferating S1 cells, cultured for five days or less, and differentiated S1 cells, cultured for 10 days or more, we compared the average radial position of the distribution maxima, shown by the vertical black line in Figure 2. The p-value between days 5 and 10 was 0.023, indicating significant difference between the distributions at those days. Thus, these results quantitatively confirmed our initial visual observation that acinar morphogenesis is accompanied by the reorganization of NuMA foci (5).

The distribution of NuMA bright features in malignant T4-2 cells differs from both proliferating and differentiated non-neoplastic S1 cells.

In proliferating S1 cells, NuMA distribution is more diffuse than in growth-arrested (day 5 of 3D culture) and fully differentiated (day 10 of 3D culture) acinar cells. We asked whether the diffuse distribution of NuMA was a characteristic of a cell population that was actively proliferating, regardless of whether or not it was malignant. As expected, immunostaining of malignant T4-2 cells for NuMA after 10 days of 3D culture showed that this protein was mostly diffusely distributed (Fig. 3), and that overall this distribution did not appear to be visually different from that observed in proliferating non-neoplastic S1 cells. To quantitatively assess this visual observation, we applied the radial-LBF analysis to 3D cultures of T4-2 cells as a function of time up to 11 days. During this culture period, T4-2 cells formed disorganized tumor-like nodules of increasing sizes. In contrast to non-neoplastic S1 cells, the radial-LBF analysis showed a fairly flat distribution of NuMA bright features in malignant cells, regardless of the number of days in 3D culture (Fig. 4a). Thus, despite the increase in mass, there were no significant alterations in the phenotype of tumor nodules during 11 days of 3D culture, and there

was no apparent change in the density of NuMA bright features in the nuclei of tumor cells during the entire culture period.

The distribution curves of the density of bright features of NuMA in T4-2 cell nuclei did not show a clear peak at any of the time points, suggesting that there was a difference in NuMA distribution not only between malignant T4-2 cells and acinar S1 cells, but also between malignant T4-2 cells and proliferating S1 cells. To better visualize the differences in the distribution of the bright features of NuMA for the different phenotypes at the time points described above, we plotted the cumulative density of NuMA bright features that exceeded unity as a function of the distance from the nuclear boundary. The cumulative plots unambiguously show that the distribution of the bright foci of NuMA is consistently similar for the different culture time points of the malignant T4-2 cells and that such a distribution is remarkably different from any of the stages of acinar morphogenesis for S1 cells, including the proliferation phase (Fig. 4b). To establish the statistical significance of the differences measured for NuMA distribution between S1 and T4-2 cells, we calculated the p-values of the average maxima accumulation. Figure 4b shows that the average maximum accumulation in S1 cells lies greater than seven standard deviations away from the average maximum accumulation for T4-2 cells. This results in a p-value of less than 0.001, indicating that the distributions for S1 and T4-2 cells are significantly different.

Discussion

We have developed an automated image analysis method that quantifies the radial distribution of nuclear proteins, on a per nucleus basis. Although the focus here has been the analysis of NuMA distribution, the tools developed are expected to be fully applicable to many

other nuclear proteins. The analysis identified individual nuclei within an image, revealed bright features of NuMA staining within each nucleus, and calculated the relative density of the bright features of NuMA staining as a function of the distance from the perimeter of the nucleus to its center. The results demonstrate quantitatively that the organization of NuMA is dynamic, and is linked directly to the phenotype of the HMECs. During the process of acinar morphogenesis, there is a marked decrease in the relative density of NuMA bright features at the perimeter of the nucleus and a marked increase in this same parameter towards the center of the nucleus. In contrast, the relative density of NuMA is more uniformly distributed in malignant cells and there is no measurable variation in its distribution during the growth of tumor-like nodules. Furthermore, the distribution of NuMA in malignant cells is clearly different from that in non-neoplastic cells regardless of the stage of acinar morphogenesis.

One of the key steps of the image analysis is the delineation of individual nuclei from 3D fluorescence images. To permit the analysis of large numbers of nuclei, we have developed a segmentation method that is automated. Our method builds upon approaches previously described (29,38-40). Irinopoulou and colleagues (30) used a global threshold, a distance transform, and a watershed method to segment nuclei on a per image-slice basis. Their final 3D reconstruction was then produced by implementing a rule-set to correctly join nuclei in adjacent slices. Our technique uses an adaptive threshold (29) that enables us to correct for inherent image anisotropy, and work directly in three dimensions. Then, much like Irinopoulou and colleagues, we apply a distance transform, but instead of a watershed method, we use template matching and region growing techniques, which are directed by the results of the distance transform. These techniques allow us to use the known geometry of the nuclei and produce a more accurate segmentation than an unconstrained watershed technique (41-44). Our segmentation method is

optimized with the help of tools that present a user with the raw DAPI-stained image overlaid with the corresponding segmentation mask and permit the visual scoring of the segmentation accuracy. Application of these tools shows that although some segmentation errors occur, the number of errors is insignificant compared to the number of correctly segmented nuclei. Our ongoing efforts are focused on improving the nuclear segmentation technique in order to maintain accuracy and efficiency in cases where the morphology of the nuclei is even more complex.

A major concern of using 3D confocal images for quantitative analysis is the inherent image anisotropy which is linked to the nature of image acquisition. Confocal images are more highly resolved in directions perpendicular than parallel to the optical axis. This is due to the spatial asymmetry of both the point-spread function of the excitation illumination and the microscope's "pinhole" spatial filter. Also, the collection efficiency and hence the brightness of confocal images decreases with depth into the object. The severity of this penetrative loss depends on the physical properties of the object, the mounting medium, and the objective lens. Standard image analysis techniques are often based on ideal imaging assumptions, which neglect inherent properties of confocal images. In such cases, images must be preprocessed using restoration techniques to remove artifacts created by confocal imaging before the quantitative analysis may proceed. In contrast, our analysis techniques take inherent properties of confocal images into account and allow results from different images to be quantitatively compared, independently of variations in fluorescence staining efficiency and acquisition parameters. The LBF analysis isolates local bright and local dark features within an image using an adaptive approach where a kernel of neighboring imaging pixels is defined around each point in the image. The LBF analysis then uses the relative brightness of the neighboring pixels in the kernel

to classify each pixel. These types of non-linear techniques are powerful because they mimic human visual perception, especially the ability to isolate rare events, such as a small number of foci in a diffuse background. Furthermore, the size of the kernel sets a spatial sensitivity limit to the LBF technique and its relative dimensions can be easily adjusted to match the spatial sampling asymmetry of the microscope. Consequently, the LBF technique is not affected by the absolute brightness of an image or long scale brightness variations like penetrative loss, and restoration techniques such as background subtraction, attenuation correction, and image interpolation are not necessary.

The ability to quantify the spatial distribution of fluorescent bright cellular features has many biological applications ranging from the study of gene expression and protein movement in live cells, and the exploration of the structural aspects of cell division, to the investigation of the role of nuclear alterations in pathologies (30,31,35,45-49). We believe that the LBF analysis, which isolates local bright features, and the radial-LBF analysis, which quantifies the distribution of the bright features, are examples of powerful tools capable of measuring differences in the complex distribution of endogenously expressed nuclear proteins from 3D images acquired following simple immunostaining procedures. Radial-LBF analysis has led to findings that strongly support the concept that specific cell and tissue phenotypes are reflected by the organization of nuclear components. These findings underline the importance of reorganization within the nucleus during the differentiation process and the alterations in nuclear organization that may be associated with tumor behavior. It was not the purpose of this study to measure independently the effect of specific cellular events that may account for tumor phenotypes, like the cell cycle phase or changes in the number of chromosome, on the distribution of NuMA.

13

However, the investigation of such effects will be of great value to refine the phenotypic classification, especially when working with small numbers of cells.

We are currently developing methods to turn the ability to quantify nuclear protein distributions into a robust classification technique to define the probability that individual nuclei belong to a specific cell phenotype. We are adding new feature-extraction algorithms and focusing on the distribution of several nuclear proteins. We have also started using the LBF-based imaging techniques to investigate the remodeling of protein distributions in normal and diseased cells in clinically-derived tissue samples. Our goal is to create a new quantitative 3D "view" of cells and tissues, based on the remodeling of nuclear proteins that helps understand the organization of the nucleus and aids in the classification of pathological samples.

Materials and Methods

Cell culture

HMT-3522 non-neoplastic (S1) cells (18) and HMT-3522 malignant T4-2 cells (19) were cultured in serum-free H14 medium as described (17,20). To induce acinar morphogenesis, S1 cells were cultured in 3D for up to 12 days on 40 μl/cm^2 Matrigel^{TM} (BD Biosciences)-coated surfaces in the presence of culture medium containing 5% Matrigel (10). Tumor-like nodule formation was achieved by culturing T4-2 cells under similar conditions but for a maximum of 11 days in order to avoid overgrowth.

Immunostaining and image acquisition

3D cultures of S1 and T4-2 cells in 4-well chamber slides were permeabilized with 0.5% peroxide and carbonyl-free triton X-100 (Sigma Biosciences) in cytoskeleton buffer (100 mM NaCl, 300 mM sucrose, 10 mM pipes, pH6.8, 5 mM MgCl$_2$) containing protease and phosphatase inhibitors (1 mM pefabloc, 10 μg/ml aprotinin, 250 μM NaF), prior to fixation in 4% paraformaldehyde and immunostaining (5). Primary monoclonal antibodies against NuMA were from clone 204.4 (Oncogene Research products) and B1C11 (a gift from Dr. Jeffrey Nickerson, University of Massachusetts). Secondary antibody was Texas-red conjugated (Jackson ImmunoResearch Laboratories). Nuclei were counterstained with 4', 6-diamidino-2-phenylindole (DAPI). Following immunostaining, 3D cultures were mounted in anti-fade medium (ProLong®, Molecular Probes) under #1 coverglass. Optically sectioned images of DAPI-stained DNA and Texas Red-labeled NuMA were acquired sequentially throughout the volume of the acini and assembled into three-dimensional images. DAPI and Texas Red signals

were acquired simultaneously into separate channels using a Zeiss 410 Confocal Laser Scanning Microscope with a planapochromatic 63x, 1.4 NA objective. The resulting voxel dimensions of the three-dimensional images was 0.08μm x 0.08μm in the plane of the slide and 0.5μm along the optical direction.

Segmentation of Individual Nuclei

To isolate individual nuclei in the three-dimensional DAPI-stained image, a model-based automatic nuclear segmentation method was developed on the assumption that nuclei of epithelial cells are of simple geometry in that they encompass a single spherical core. An adaptive threshold was first applied to the DAPI-stained image to produce the binary segmentation mask of the nuclei. The technique, which normalizes for penetrative loss along the optical direction, uses a difference-of-Gaussians filter (50) followed by a morphological closing filter and a flood-fill algorithm (41-44). While this technique accurately delineates nuclei from their background, it does not completely separate neighboring nuclei when they are tightly clustered. To separate nuclei that are connected by the binary mask, the central core of each nucleus was located, using standard template matching techniques, and dilated into the rest of the nucleus using standard region-growing techniques (41-44). Briefly, a template was constructed with dimensions that approximated those of the average spherical core of nuclei and was convolved with the binary nuclear mask. This convolution produced a map that indicated the percentage of the template that fit within the binary mask at each point in the image. Then, the template was stamped into the binary mask at locations where there were corresponding local maxima in the map that exceeded 70%. The templates were stamped at the center-of-mass of the local maximum, in an order ranked by their percentage, starting from the highest. A template was

not stamped if the local maximum was less than 70%, if it overlapped a previously stamped template by more than 70%, or if the local maximum was at the boundary of the binary mask. Once all the nuclear cores were located, each template was dilated in a semi-intelligent fashion. The template dilation was done independently in the positive and negative X, Y, and Z directions. Dilation along any direction was halted when 60% of the dilating template boundary reached the boundary of the binary mask. This prevented a dilating template from squeezing through narrow regions in the binary mask that connected two adjacent nuclei. Also, dilation was stopped in all directions if the volume of the dilated template exceeded nine times its original volume. This phenomenon occurred if nuclei were clustered so closely that the initial segmentation mask failed to separate them adequately. The resulting object was reported as an under-segmentation error.

Distribution Analysis of NuMA

Following immunostaining, image acquisition and nuclear segmentation, NuMA bright features were first isolated by the LBF analysis technique and then their radial distribution calculated by our radial-LBF technique. In the LBF analysis, pixel brightness in the raw NuMA images was normalized by the local average brightness using an extension of the difference-of-Gaussians technique (50). The raw NuMA image was masked by the binarized segmentation result derived from the DAPI image as described above. Then, the image brightness within each nucleus was rescaled by dividing the brightness at each point by the average brightness within a local region surrounding that point. The dimension of the local region was chosen to be half that of the dimension of the nuclear core. This choice resulted in a local region that was significantly larger than the bright NuMA foci of interest but smaller than the nuclear dimension. This was

important because the LBF technique sensitively resolves light or dark features that lie within the local region while ignoring features that are larger. Using this approach allowed the bright foci and dark regions of interest within the nucleus to be resolved and the low-frequency brightness variations, due to nuclear geometry and finite axial resolution, to be correctly normalized. In the resulting LBF images, bright image features have values above unity while dark image features have values below unity. For the radial-LBF analysis, a distance transform (41-44) was applied to the nuclear segmentation mask. The transform calculates the shortest distance of each point within a nucleus to the nuclear boundary and in doing so, divides each nucleus into a set of concentric terraces of equal thickness. The LBF image was then used in conjunction with the nuclear segmentation mask and the distance transform to compute the density of local bright features in each terrace of each nucleus (see Fig. 1a). In each terrace, the density was calculated as the number of pixels in local bright features divided by the total number of pixels. The relative distribution of the density of bright features within each nucleus was revealed by normalizing the density per terrace, so that the average density of bright features was unity for each nucleus. The distances defined by the distance transform were also normalized so that the distance at the nuclear perimeter was 0 and the distance at the center of the nucleus was 1.0. This normalization was done to account for variation in the number of terraces per nucleus due to variations in nucleus size and shape. Finally, normalized density of bright features was plotted against normalized distance from the perimeter of the nucleus to its center.

Statistical Analysis

P-values were derived from the standard normal distribution using the z-score ($Z=(X-\mu)/\sigma$). Two averages with a p-value less than 0.05 were considered significantly different.

Acknowledgements

References

1. Lelièvre, S.A., Bissell, M. J. & Pujuguet, P. (2000) *Crit. Rev. Eukaryot. Gene Expr.* **10**, 13-20.

2. Dillon, N., & Festenstein, R. (2002) *Trends Genet.* **18**, 252-258.

3. Mancini, M.A., He, D., Ouspenski, I.I., & Brinkley, B. R. (1996) *J. Cell Biochem.* **62**, 158-164.

4. Gerlich, D., Beaudouin, J., Gebhard, M., Ellenberg, J., & Eils, R. (2001) *Nat. Cell Biol.* **3**, 852-855.

5. Lelièvre, S.A., Weaver,V.M. Nickerson,J.A. Larabell,C.A. Bhaumik,A. Petersen,O.W. & Bissell, M.J. (1998) *Proc. Natl. Acad. Sci.* USA **95**, 14711-14716.

6. Antoniou, M., Carmo-Fonseca, M., Ferreira, J., & Lamond, A. I. (1993) *J. Cell Biol.* **123**, 1055-1068.

7. Beil, M., D. Durschmied, S. Paschke, B. Schreiner, U. Nolte, A. Bruel, & T. Irinopoulou. (2002) *Cytometry*. **47**, 217-225.

8. Gribbon, C., Dahm, R., Prescott, A. R., & Quinlan R. A. (2002) *Eur. J. Cell Biol*. **81**, 557-566.

9. Cammas, F., Oulad-Abdelghani, M., Vonesch, J. L., Huss-Garcia, Y., Chambon, P., Losson, R. (2002). *J. Cell Sci.* **115**, 3439-3448.

10. Plachot, C., & Lelièvre, S. A. (2004) *Exp. Cell Res.* **298**, 122-132.

11. Powers, M. J., Janigian, D. M., Wack, K. E., Baker, C. S., Beer Stolz, D., & Griffith, L. G. (2002) *Tissue Eng.* **8**, 499-513.

12. Gudjonsson, T., Ronnov-Jessen, L., Villadsen, R., Bissell, M. J., & Petersen, O. W. (2003) *Methods* **30**, 247-255.

13. Jacks, T., & Weinberg, R. A. (2002) *Cell* **111**, 923-925.

14. Bissell, M. J., Weaver, V. M., Lelievre, S. A., Wang, F., Petersen, O. W., & Schmeichel, K. L. (1999) *Cancer Res*. **59**, 1757-1763.

15. Bissell, M.J., Rizki, A., & Mian, S. (2003) *Curr. Opin. Cell Biol*. **15**, 753-762.

16. Weaver, V. M., Lelievre, S., Lakins, J. N., Chrenek, M. A., Jones, J. C., Giancotti, F., Werb, Z. & Bissell, M. J. (2002) *Cancer Cell*. **2**, 205-216.

17. Petersen, O.W., Ronnov-Jessen, L., Howlett, A. R., & Bissell, M. J. (1992) *Proc. Natl. Acad. Sci.* USA **89**, 9064-9068.

18. Briand, P., Petersen, O. W., & Van Deurs. B. (1987) *In Vitro Cell Dev. Biol.* **23**, 181-188.

19. Briand, P., Nielsen, K. V., Madsen, M. W. & Petersen, O. W. (1996) *Cancer Res*. **56**, 2039-2044.

20. Weaver, V. M., Petersen, O. W., Wang, F., Larabell, C. A., Briand, P., Damsky,C., & Bissell, M. J. (1997) *J. Cell Biol*. **137**, 231-245.

21. Weaver, V. M., Carson, C. E. Walker, P. R., Chaly, N. Lach, B., Raymond, Y., Brown, D. L. & Sikorska, M. (1996) *J. Cell Sci*. **109**, 45-56.

22. Zweyer, M., Riederer, B. M., Ochs, R. L., Fackelmayer, F. O., Kohwi-Shigematsu, T., Bareggi, R., Narducci, P., & Martelli, A. M. (1997) *Exp. Cell Res.* **230**, 325-336.

23. Mattagajasingh, S. N., Huang, S. C., Hartenstein, J. S., Snyder, M., Marchesi, V. T., & Benz, E. J. (1999) *J. Cell Biol.* **145**, 29-43.

24. Merdes, A., & Cleveland, D.W. (1998) *J. Cell Sci*. **111**, 71-79.

25. Sodja, C., Walker, P. R., Brown, D. L., & Chaly, N. (1997) *Biochem Cell Biol.* **75**, 399-414.

26. Gil, J., & Wu, H. S. (2003) *Cancer Invest.* **21**, 950-959.

27. Zink, D., Fische, A. H., & Nickerson, J. A. (2004) *Nat. Rev. Cancer*. **4**, 677-687.

28. Shumaker, D.K., Kuczmarski, E. R. & Goldman, R.D. (2003) *Curr. Opin. Cell Biol*. **15**, 358-366.

29. Ancin, H., Roysam, B., Dufresne, T. E., Chestnut, M. M., Ridder, G. M., Szarowski, D. H., & Turner, J. N. (1996) *Cytometry* **25**, 221-234.

30. Irinopoulou, T., Vassy, J., Beil, M., Nicolopoulou, P., Encaoua, D., & Rigaut, J. P. (1997) *Cytometry* **27**, 99-105.

31. Lieb, J. D., Ortiz de Solorzano, C., Rodriguez, E. G., Jones, A., Angelo, M., Lockett, S., & Meyer, B. J. (2000) *Genetics* **156**, 1603-21.

32. Schupp, S., Elmoataz, A., Herlin, P., & Bloyet, D. (2001) *Anal. Quant. Cytol. Histol.* **23**, 257-267.

33. Beil, M., Durschmied, D., Paschke, S., Schreiner, B., Nolte, U., Bruel, A., & Irinopoulou, T. (2002) *Cytometry* **47**, 217-225

34. Eils, R., & Athale, C. (2003) *J. Cell Biol.* **161**, 477-481.

35. Voss, T. C., Demarco, I. A., Booker, C. F., & Day, R. N. (2004) *Biotechniques* **36**, 240-247.

36. Swedlow, J. S., Goldberg, I., Brauner, E., & Sorger, P. (2003) *Science* **300**, 100-102.

37. Ecker, RC, & Steiner GE. (2004) *Cytometry* **59A**, 182-190.

38. Rigaut, J. P., Vassy, J., Herlin, P., Duigou, F., Masson, E., Briane, D., Foucrier, J., Carvajal-Gonzalez, S., Downs, A. M., & Mandard, A. M. (1991) *Cytometry* **12**, 511-524.

39. Belien, JA, van Ginkel HA, Tekola P, Ploeger LS, Poulin NM, Baak JP, & van Diest PJ. (2002) *Cytometry* **49**, 12-21.

40. Lin, G., Adiga, U., Olson, K., Guzowski, J. F., Barnes, C. A., & Roysam, B. (2003) *Cytometry* **56A**, 23-36.

41. Castleman, K. R. (1996) *Digital Image Processing* (Prentice-Hall)

42. Russ, J. C. (1992) *The Image Processing Handbook* (CRC Press)

43. Jahne, B. (2002) *Digital Imaging Processing* 5th ed. (Springer)

44. Soille, P. (2003) *Morphological Image Analysis* 2nd ed. (Springer)

45. Tvarusko, W., Bentele, M., Misteli, T., Rudolf, R., Kaether, C., Spector, D. L., Gerdes, H. H., & Eils, R. (1999) *Proc. Natl. Acad. Sci.* USA **96**, 7950-7955.

46. Eils, R., Gerlich, D., Tvarusko, W., Spector, D. L., & Misteli, T. (2000) *Mol. Biol. Cell.* **11**, 413-418.

47. Platani, M., Goldberg, I., Swedlow, J. R., & Lamond, A. I. (2000) *J. Cell Biol.* **151**, 1561-1574.

48. Kyan, M. J, Guan, L., Arnison, M. R., & Cogswell, C. J. (2001) *IEEE Trans. Biomed. Eng.* **48**, 1306-1318.

49. Chin, K., Ortiz de Solorzano, C., Knowles, D., Jones, A., Chou, W., Rodriguez, E. G., Kuo, W. L., Ljung, B. M., Chew, K., Myambo, K., *et al.* (2004) *Nat. Genet.* **36**, 984-988.

50. Marr, D. (1982) *Vision* (W.H.Freeman & Company)

Figure legends

Figure 1. LBF analysis of NuMA distribution from 3D images. **a**. Flowchart of the imaging processing steps including a graph of the relative density of local bright features of NuMA in 77 nuclei from the three acini depicted in Fig 1b. The radial distributions of local bright features within each nucleus in the NuMA image are calculated by first generating a segmentation mask from the image of DAPI-stained DNA. The segmentation mask not only defines the extent of each nucleus, but it is also used to define a set of radial steps within each nuclear volume. The graph shows the mean and standard deviation of the relative density of NuMA bright features extracted by LBF analysis (ordinate) as a function of the relative distance from the perimeter (0.0) to the center (1.0) of the nuclei (abscissa). **b-h**. Distribution density of the bright features of NuMA in acinar cells. S1 HMECs were cultured in 3D to induce acinar morphogenesis. Each panel corresponds to the application of the different steps of distribution analysis starting from the same original image. **b.** Fluorescence micrograph of DAPI-stained nuclei from a single optical section containing three acini [1;2;3]. **c.** Fluorescence micrograph of Texas-red immunolabeled NuMA from the optical section corresponding to the DAPI image shown in **a**. **d.** Segmentation mask derived from the DAPI-stained image showing a single slice of individually enumerated nuclei. **e.** Composite view of the local bright features (light gray) extracted by the LBF analysis overlaid with the segmentation mask (dark gray). **f.** Concentric terraces resulting from the application of the distance transform on the segmentation mask.

Figure 2. Average relative density of local bright features of NuMA during acinar

morphogenesis. S1 cells were cultured in 3D for 3, 5, 10 and 12 days. Plots represent the relative density of NuMA bright features extracted by LBF analysis (ordinate) of a population of nuclei as a function of the relative distance from the perimeter (0.0) to the center (1.0) of the nuclei (abscissa) for each time point. Vertical lines (black) represent the location of the peak of bright feature density in the nucleus. Horizontal lines (gray) represent the extent of nuclear volume with densities of bright features above the average. The number of days the cells were in culture and the number of nuclei analyzed are indicated above each corresponding graph. Bars represent the standard deviations of the relative density of NuMA bright features calculated from multicellular units of the same phenotype, on a per image basis.

Figure 3. Immunostaining of NuMA in acinar S1 and malignant T4-2 HMECs. S1 and T4-2 cells were cultured in 3D for 10 days. Each image shows an optical section through the center of the nucleus of NuMA immunostaining in acinar S1 cells (left) and malignant T4-2 cells (right). One nucleus is shown per image. Arrows indicate typical empty areas in NuMA staining at the periphery of the nucleus of the S1 cell. Size bar = 2 μm.

Figure 4. Differences in the relative density of NuMA bright features between non-neoplastic and malignant cells. **a.** T4-2 cells were cultured in 3D for 4, 5, 10 and 11 days. Plots represent the relative density of NuMA bright features extracted by LBF analysis (ordinate) of a population of nuclei as a function of the relative distance from the perimeter (0.0) to the center (1.0) of the nuclei (abscissa) for each time point. Vertical lines (black) represent the location of the peak of bright feature density in the nucleus. Horizontal lines (gray) represent the extent of nuclear volume with densities of bright features above the average. The number of days the cells

25

were in culture and the number of nuclei analyzed are indicated above each corresponding graph.

b. Cumulative plots of the relative density of NuMA bright features above unity (ordinate) at different time points of 3D culture of S1 and T4-2 cells as a function of the relative distance from the perimeter (0.0) to the center (1.0) of the nucleus (abscissa). Cumulative plots for S1 and T4-2 cells were prepared from the relative density data shown in figures 2 and 4a, respectively. Bars represent the standard deviations of the relative density of NuMA bright features calculated from multicellular units of the same phenotype, on a per image basis.
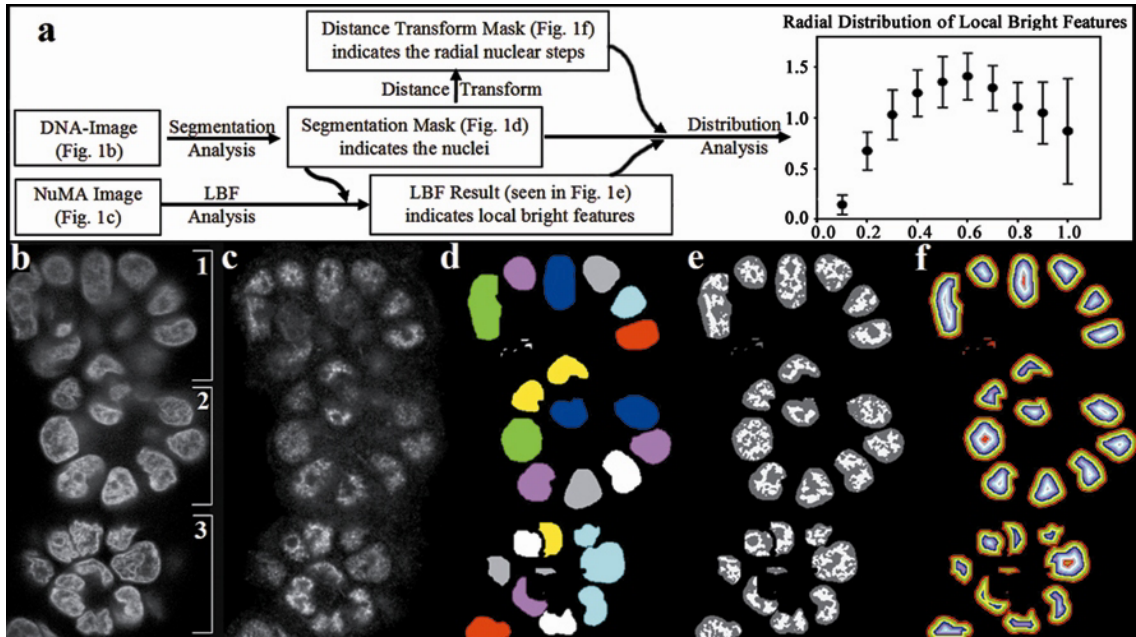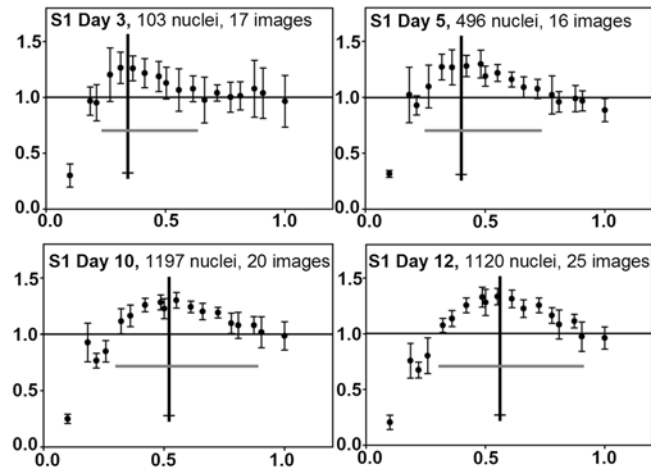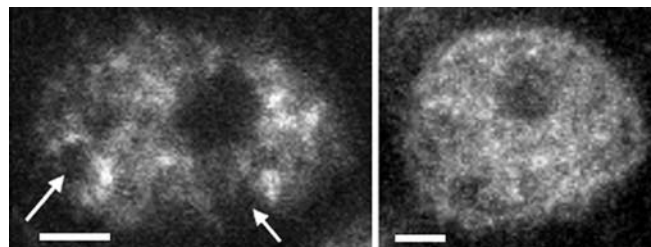
Figure 1:

Figure 2:

Figure 3:

Figure 4: